Ab initio study of the band structures of different phases of higher manganese silicides

D. B. Migas,* V. L. Shaposhnikov, A. B. Filonov, and V. E. Borisenko
Belarusian State University of Informatics and Radioelectronics, P.Browka 6, 220013 Minsk, Belarus

N. N. Dorozhkin
Belarusian State University, Nezavisimosti Av. 4, 220050 Minsk, Belarus

(Received 16 November 2007; revised manuscript received 14 January 2008; published 25 February 2008)

By means of first principles calculations, we have investigated the band structures of different phases of higher manganese silicides ($MnSi_x$ with x ranging from 1.73 to 1.75). In this family, $Mn_{11}Si_{19}$, $Mn_{15}Si_{26}$, and $Mn_{27}Si_{47}$ have been found to behave like degenerate semiconductors and, at the same time, like metals because the Fermi level stays partly in the energy gap and partly in the valence band close to its top. The spin-polarized calculations have revealed that these phases can be also treated as half-metals displaying 100% spin polarization of holes at the Fermi energy. On the contrary, Mn_4Si_7 is shown to be a semiconductor with the indirect band gap of 0.77 eV. Its dielectric function possesses some anisotropy effects with respect to different light polarizations. We have also discovered that the $MnSi_{1.75}$ stoichiometry provides semiconductor properties without degeneracy. The role of stacking faults in the gap reduction of higher manganese silicides is discussed.

DOI: 10.1103/PhysRevB.77.075205 PACS number(s): 71.20.Nr, 78.20.Bh, 75.50.Pp

I. INTRODUCTION

Semiconducting silicides have attracted much attention because of their prospects for optoelectronic and thermoelectric applications.[1] Among them, iron disilicide (β-$FeSi_2$) is one of the most promising and well studied both experimentally and theoretically.[1] However, in the case of higher manganese silicides (HMSs) ($MnSi_x$ with $x \simeq 1.73-1.75$), also indicated to have promising properties,[1] there are several issues which are not fully understood and explored: the existence of different phases with similar crystal structures and the value and the character of the gap in addition to the reported degenerate semiconducting nature and observed metallic behavior as a magnetic system. In fact, HMSs were shown to have several phases with slightly different stoichiometry (see Table I) such as Mn_4Si_7,[2] $Mn_{11}Si_{19}$,[3,4] $Mn_{15}Si_{26}$,[5] and $Mn_{27}Si_{47}$.[6] They all derived from the $TiSi_2$ structure[7] and displayed the tetragonal crystal structure with almost equal a lattice parameters and unusually long c lattice parameters (Table I). The corresponding unit cells of HMSs are shown in Fig. 1. Moreover, HMSs are also characterized by the same building principle as determined by the high-resolution electron microscopy study.[7] Thus, Mn atoms occupy Ti sites and form the Mn sublattice, while Si atoms in a double-helical arrangement form another sublattice by filling intersites in the Mn sublattice. A commensurate match of the two sublattices requires such a long c lattice parameter. However, it is hard to distinguish between different phases of HMS.[7,8]

From the other side, resistivity of HMS indicates the behavior usually observed for degenerate semiconductors: at temperatures below 500 K, the resistivity increases with temperature, while above 500 K, the resistivity starts decreasing exponentially indicating the gap of about 0.4 eV.[9,10] The Hall effect measurements identify holes to be the dominant carriers in the whole temperature range,[9–11] and the hole mobility is shown to be very small.[8–11] The band gaps for bulk samples were found to scatter from 0.4 eV (Ref. 9) to 0.7 eV (Ref. 11) and to 0.9 eV.[12] In addition, the gaps of 0.40 and 0.42 eV have been obtained on thin film samples according to resistivity and the Hall effect experiments, respectively.[10] Bost and Mahan[13] by analyzing the absorption coefficient data have shown that polycrystalline films of HMS were characterized by the direct transition of 0.68 eV with a strong free carrier absorption below 0.2 eV. The same band gap was derived from their resistivity measurements.[13] Another optical investigation[14] carried out on a single layer of HMS has determined the direct band gap between 0.78

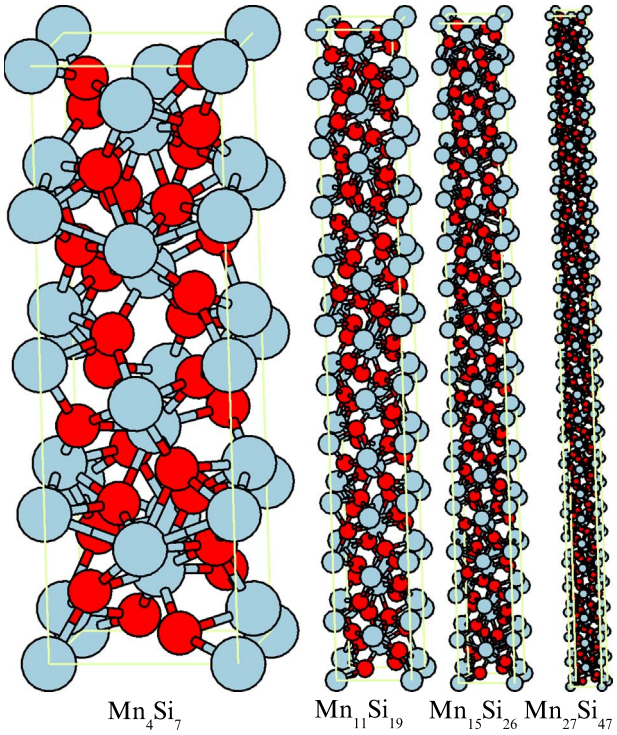

FIG. 1. (Color online) The unit cells of HMS. The larger gray (blue) balls stand for Mn atoms, while the smaller dark (red) balls indicate Si atoms.

 ©2008 The American Physical Society

and 0.83 eV. On the contrary, Teichert *et al.*[8] have found the indirect band gap of 0.46 eV along with the first direct transition of 0.78 eV by means of absorption measurements. Very similar results have been obtained by Rebien *et al.*[15] when investigating absorption coefficient: the indirect and the lowest direct transitions were shown to be 0.40 and 0.96 eV, respectively. In the latter case, the epitaxially grown thin films of HMS were studied. In addition, Mn_4Si_7 was reported to be a weak itinerant magnetic system displaying the saturation magnetization of $0.012\mu_B$/Mn below 40 K.[2]

To the best of our knowledge, there was no attempt to perform theoretical calculations of electronic and optical properties of HMS in order to shed some light on semiconducting and/or metallic nature of these materials. In this paper, we present the band structures (nonmagnetic and magnetic cases), the density of states (DOS), and the dielectric function of different phases of HMS obtained by *ab initio* calculations. Eventually, an interpretation on the existing experimental data is provided.

II. COMPUTATIONAL DETAILS

Full structural optimization of HMS has been performed by the first principles total energy code VASP with plane-wave basis set and ultrasoft pseudopotentials (USPPs) described in detail elsewhere.[16–18] In our study, we applied exchange and correlation potentials using the generalized gradient approximation (GGA) of Perdew and Wang.[19] Total energy minimization, via an optimization of lattice parameters and a relaxation of atomic positions in a conjugate gradient routine, was obtained by calculating the Hellmann–Feynman forces and the stress tensor. The Pulay corrections have been included in order to compensate for changes of the basis set due to a variation in the shape of the unit cell. We have used the energy cutoff of 320 eV. The $12\times12\times4$ grid of the Monkhorst–Pack points was utilized in the case of Mn_4Si_7. Because of the relatively large c lattice parameter (see Table I and Fig. 1), for $Mn_{11}Si_{19}$ and $Mn_{15}Si_{26}$, we used the $6\times6\times1$ grid, while for $Mn_{27}Si_{47}$, the **k**-point mesh was set to $2\times2\times1$. The calculation of band structures was performed on the obtained self-consistent charge densities.

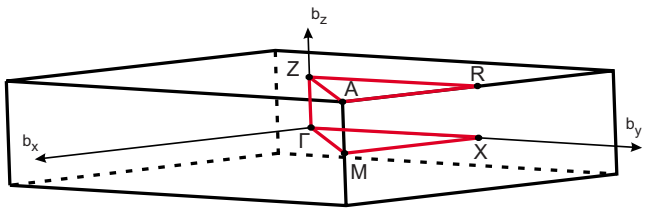

FIG. 2. (Color online) The simple tetragonal Brillouin zone.

The electronic band structure, the total and projected DOS, and the dielectric function of Mn_4Si_7 have been calculated by using WIEN2K package,[20] which is a full potential linearized augmented plane-wave (FLAPW) method. We applied GGA of Perdew and Wang[19] along with the structural parameters of Mn_4Si_7 fully optimized by USPP. The self-consistent procedure has been carried out with the energy cutoff constant $R_{mt}K_{max}=8$ and on mesh of 30 **k** points in the irreducible part of the simple tetragonal Brillouin zone (BZ). The corresponding BZ is shown in Fig. 2. Further increase in the cutoff value, basis set, and **k**-point number did not lead to any noticeable changes in the eigenvalues. The integration

TABLE I. Experimental and theoretical lattice parameters [a and c (Å)], the number of Mn (n_{Mn}) and Si (n_{Si}) atoms in the unit cell, and the stoichiometry ($n_{Si/Mn}$) of different phases of HMS. The s.f. and s.p. stand for the stacking fault and spin-polarized cases, while $2b$, $4f$, and $4b$ indicate the Wyckoff position of the Si adatom in the unit cell. The experimental lattice parameters for Mn_4Si_7, $Mn_{11}Si_{19}$, $Mn_{15}Si_{26}$, and $Mn_{27}Si_{47}$ are from Refs. 2 and 4–6, respectively.

	Mn_4Si_7				$Mn_{15}Si_{26}$			
	Expt	Theory	Theory s.f.	Theory s.f. s.p.	Expt	Theory	Theory Si ($4b$)	Theory s.p.
a	5.526	5.510	5.522	5.525	5.531	5.502	5.518	5.503
c	17.517	17.418	34.998	35.126	65.311	65.284	65.267	65.293
n_{Mn}	16	16	32	32	60	60	60	60
n_{Si}	28	28	56	56	104	104	105	104
$n_{Si/Mn}$	1.75	1.75	1.75	1.75	1.733	1.733	1.75	1.733
	$Mn_{11}Si_{19}$					$Mn_{27}Si_{47}$		
	Expt	Theory	Theory Si ($2b$)	Theory Si ($4f$)	Theory s.p.		Expt	Theory
a	5.530	5.500	5.521	5.519	5.499		5.530	5.494
c	47.763	47.881	47.857	47.913	47.877		117.9	117.731
n_{Mn}	44	44	44	44	44		108	108
n_{Si}	76	76	77	77	76		188	188
$n_{Si/Mn}$	1.727	1.727	1.75	1.75	1.727		1.741	1.741

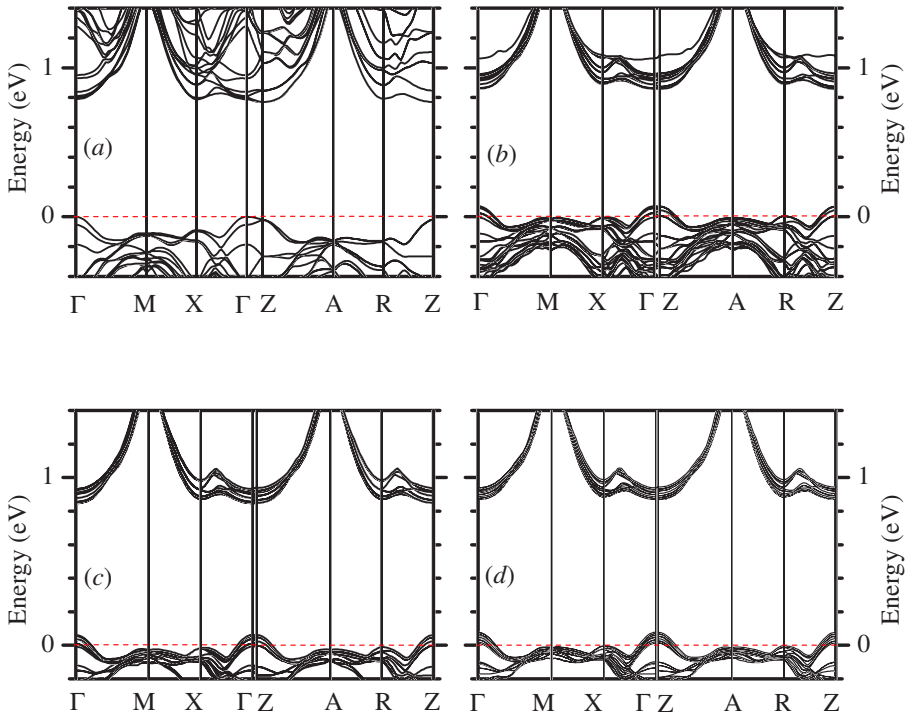

FIG. 3. (Color online) The band structures of (a) Mn_4Si_7, (b) $Mn_{11}Si_{19}$, (c) $Mn_{15}Si_{26}$, and (d) $Mn_{27}Si_{47}$. Zero at the energy scale corresponds to the Fermi energy.

on the BZ was performed by the tetrahedron method with the Blöchl corrections. For a band structure representation, we choose up to 30 **k** points for any high-symmetry direction. The dense mesh of 680 **k** points was generated to calculate total and projected DOSs as well as dipole matrix elements for evaluation of the imaginary (ε_2) and real (ε_1) parts of the dielectric function. The effective mass tensors for holes and electrons were evaluated along the principal axes of the ellipsoidal energy surface in the band extrema by calculating the appropriate second derivatives within the five-point approximation.

III. RESULTS AND DISCUSSION

A. Role of stoichiometry on degeneracy in semiconducting properties of higher manganese silicide

The band structures of the Mn_4Si_7, $Mn_{11}Si_{19}$, $Mn_{15}Si_{26}$, and $Mn_{27}Si_{47}$ phases as calculated by USPP along some high-symmetry directions of the simple tetragonal BZ (Fig. 2) are shown in Fig. 3. It is evident that Mn_4Si_7 [Fig. 3(a)] is a semiconductor because the Fermi level stays in the gap. On the contrary to Mn_4Si_7, the other phases of HMS, namely, $Mn_{11}Si_{19}$, $Mn_{15}Si_{26}$, and $Mn_{27}Si_{47}$, have turned out to be metals [Figs. 3(b)–3(d)] because the Fermi level crosses some bands regardless of the presence of the energy gap. Nevertheless, the latter phases can also be treated as degenerate *p*-type semiconductors due to the fact that the Fermi level is partly inside the valence band dividing it into occupied and unoccupied parts and partly in the energy gap. In the case of $Mn_{11}Si_{19}$, the number of the valence electrons is 612 indicating that the Fermi level should be between the 306th and 307th bands, whereas the energy gap in the band structure is between the 308th and 309th bands as if two top valence bands were virtually unoccupied. The same issue (two virtually unoccupied top valence bands) is observed for $Mn_{15}Si_{26}$ and $Mn_{27}Si_{47}$. Our findings can easily explain the experimentally observed degenerate nature of semiconducting properties of HMS. In fact, at low temperatures, the metalliclike behavior of the increasing resistivity with temperature[2,8–11] is attributed to the existence of the unoccupied part of the valence band acting as the conduction band. At higher temperatures, the thermal activation is capable of transferring an electron from the valence band to the conduction band via the energy gap providing the decrease in the resistivity[9–11] typical of a semiconducting material. To this end, we would like to point out that the concentration of free carriers in degenerate HMS is limited to four holes per unit cell. Our estimates of the hole concentration are 1.1×10^{21}, 2.0×10^{21}, and 2.7×10^{21} cm^{-3} for $Mn_{27}Si_{47}$, $Mn_{15}Si_{26}$, and $Mn_{11}Si_{19}$, respectively. These values, being an order of magnitude lower than in metals, are very well comparable with the experimentally determined ones, -2×10^{20},[8] 7.1×10^{20},[10] 2.1×10^{21},[11] and 2.3×10^{21} cm^{-1}.[9]

One possible way to fill completely the valence band and to shift the Fermi level to the energy gap can be four electrons or one Si atom which should be added to the unit cell of $Mn_{11}Si_{19}$, $Mn_{15}Si_{26}$, and $Mn_{27}Si_{47}$. The unit cell of $Mn_{11}Si_{19}$ contains the unoccupied 2*b* and 4*f* Wyckoff positions:[4] in the case of $Mn_{15}Si_{26}$, the 4*b* Wyckoff position,[5] while for $Mn_{27}Si_{47}$, the 2*b* and 2*d* Wyckoff positions.[6] In the cases of $Mn_{11}Si_{19}$ and $Mn_{15}Si_{26}$, we have added one Si atom to the unit cell and the corresponding band diagrams are reported in Figs. 4(a)–4(c). These new phases with the addi-

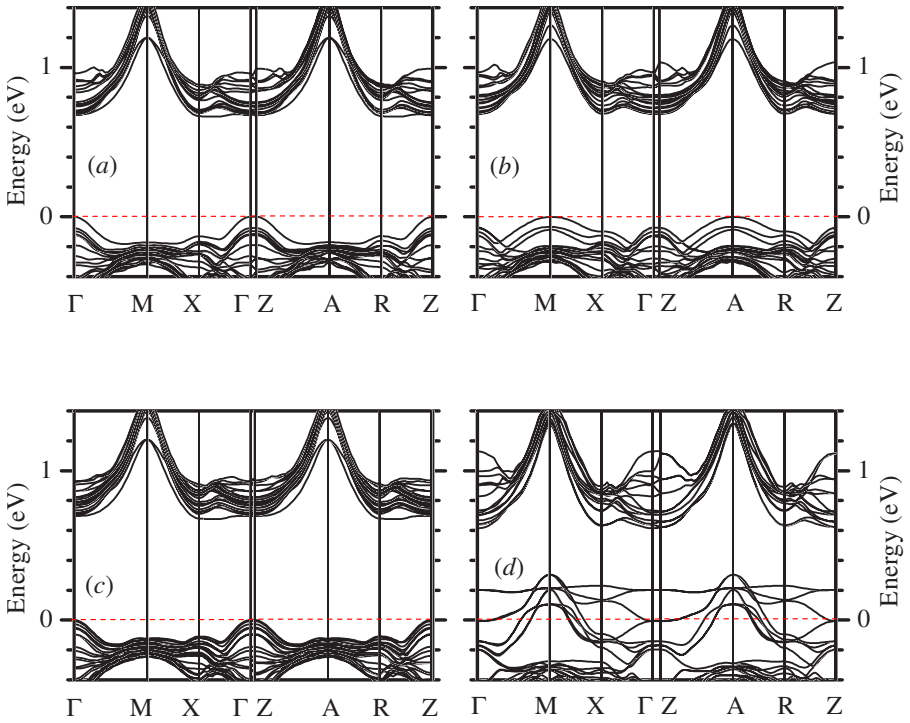

FIG. 4. (Color online) The band structures of (a) $Mn_{11}Si_{19}+1Si$ atom per unit cell in the 2*b* Wyckoff position, (b) $Mn_{11}Si_{19}+1Si$ atom per unit cell in the 4*f* Wyckoff position, (c) $Mn_{15}Si_{26}+1Si$ atom per unit cell in the 4*b* Wyckoff position, and (d) Mn_4Si_7 with stacking faults. Zero at the energy scale corresponds to the Fermi energy.

tional Si atom do not display the degenerate nature because the Fermi level is in the band gap. We also believe that the $Mn_{27}Si_{47}$ phase follows the same trend. Moreover, our calculations have also revealed the $Mn_{11}Si_{19}+1Si$, $Mn_{15}Si_{26}+1Si$, and Mn_4Si_7 phases to be close in total energy.

By introducing a Si atom into the unit cell of HMS, we have noticed that stoichiometry of $Mn_{11}Si_{19}+1Si$ and $Mn_{15}Si_{26}+1Si$ changes to $MnSi_{1.75}$ (see Table I). The same happens to $Mn_{27}Si_{47}+1Si$ (189/108=1.75). In our previous papers,[21,22] we have already pointed out the importance of stoichiometry in providing the semiconducting nature: only $ReSi_{1.75}$ was found to be the semiconducting phase of rhenium silicide ($ReSi_x$). This issue also indicates that semiconducting phases of silicides of Mn and Re (both elements belong to the VII column of the Periodic Table) display the same stoichiometry. In addition, in Table I, we have also summarized the optimized lattice parameters along with experimental values. It is clearly seen that the measured *a* lattice parameter is constantly larger than the calculated one for Mn_4Si_7, $Mn_{11}Si_{19}$, $Mn_{15}Si_{26}$, and $Mn_{27}Si_{47}$ even though the GGA approximation was used in our study. The latter approximation is believed to slightly overestimate lattice parameters for transition metal silicides.[23] However, in the cases of $Mn_{11}Si_{19}+1Si$ and $Mn_{15}Si_{26}+1Si$, the *a* parameter is closer to the experimental values (Table I).

B. Band structures of higher manganese silicide

Let us now consider the dispersion of the bands near the gap region of HMS in detail. The band structure of Mn_4Si_7 [Fig. 3(a)] is characterized by the indirect band gap of 0.769 eV between the valence band maximum in the Γ point and the conduction band minimum in the *Z* point. The direct transitions in Γ (0.789 eV) and *Z* (0.771 eV) are very close in energy due to flat bands along the Γ-*Z* direction also indicating that the energy difference between the direct and indirect transitions is within a few meV. There are two other minima of the conduction band in *X* and *R* close in energy to the minima in Γ and *Z*. Because of the relatively large *c* lattice parameter, the planes with the Γ, *M*, and *X* points and with the *Z*, *A*, and *R* points are not far away in the reciprocal space (Fig. 2). This issue, in turn, leads to almost the same dispersion of the bands near the gap region in both planes (compare band dispersion along the Γ-*M*-*X*-Γ and the *Z*-*A*-*R*-*Z* segments). Dispersion of the bands near the energy gap of $Mn_{11}Si_{19}$ [Fig. 3(b)], $Mn_{15}Si_{26}$ [Fig. 3(c)], and $Mn_{27}Si_{47}$ [Fig. 3(d)] is very close to that of Mn_4Si_7 [Fig. 3(a)]. In addition, the values of the energy gap are also similar and calculated to be 0.78 eV, while the Fermi level lies 0.05–0.07 eV below of the top of the valence band. The introduction of a Si atom into the unit cell of $Mn_{11}Si_{19}$ [Figs. 4(a) and 4(b)] and $Mn_{15}Si_{26}$ [Fig. 4(c)] does not sizably affect the values of the gap (about 0.68 eV), does not provide any localized states, and does not change the indirect nature of the gap. However, some variations in band dispersion can be spotted. In fact, the conduction band minimum appears in the *X* and *R* points due to the lowering of the first conduction band at *X* and *R* [see Figs. 4(a)–4(c)]. For $Mn_{11}Si_{19}+1Si$ in the 4*f* Wyckoff position, the last valence band shifts up at *M* and *A* providing the valence band maximum in these points [Fig. 4(b)].

We are aware that our calculations have not been done within the *GW* approximation and the obtained band gaps

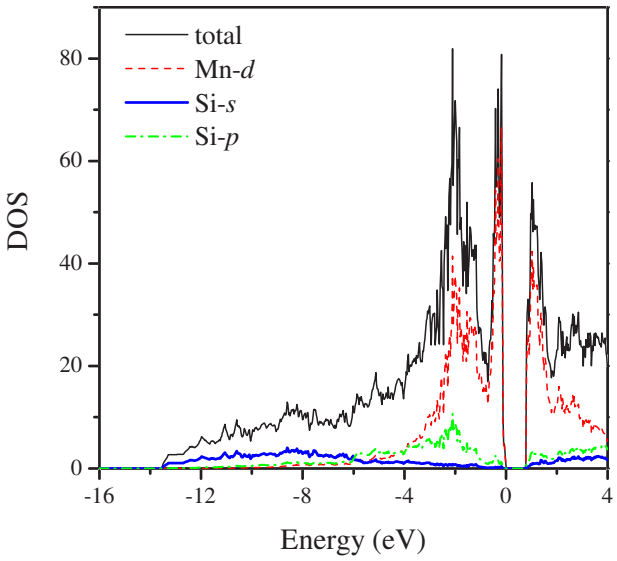

FIG. 5. (Color online) The total and projected DOS (states/eV/cell) of Mn_4Si_7. Zero at the energy scale corresponds to the Fermi energy.

are underestimated. However, the calculated values (0.68–0.77 eV) are larger than the experimentally measured ones [about 0.40 eV (see Refs. 8–10 and 15)]. Moreover, the recent optical measurements[15] on high quality samples show the indirect and the first direct transitions to be 0.40 and 0.96 eV, respectively, while our predictions indicate that several indirect and direct transitions are very close in energy. In order to clarify this issue, we have decided to trace energy gaps of HMS with stacking faults. Stacking faults are common for the $TiSi_2$ structure[24] where unit cells are rotated by 90° around the z axis with respect to each other, which is possible in a structure with the tetragonal symmetry. Thus, the band structure of Mn_4Si_7 with the doubled unit cell along the z axis and having the stacking fault is presented in Fig. 4(d). It is clearly seen that such a defect in the Mn_4Si_7 structure leads to the metallic nature along with a sizable reduction of the energy gap (0.31 eV). Even though the concentration of staking faults in our calculations is very high, we believe that this defect can locally reduce the gap and, eventually, be the origin of small band-gap values (about 0.40 eV) observed in the experiments.[8–10,15] In addition, Mn_4Si_7 with stacking faults displays the a lattice parameter to be very close to the experimental value (Table I).

C. Density of states, mobility of holes, and dielectric function of Mn_4Si_7

As far as the Mn_4Si_7, $Mn_{11}Si_{19}+1Si$, and $Mn_{15}Si_{26}+1Si$ phases of HMS have almost the same crystal structure and display similar dispersion of the bands close to the gap region, we have chosen Mn_4Si_7 in order to provide a detailed description of DOSs, effective masses of holes and electrons, the hole mobility, and the imaginary and real parts of the dielectric function. It should be mentioned here that both USPP and FLAPW methods fully agree about band dispersion near the gap region. Thus, in Fig. 5, we report the energy dependence of the total and projected DOSs for Mn_4Si_7 as calculated by the FLAPW method. The valence band can be virtually divided into three parts. The first part extends from the bottom of the valence band up to −6 eV and the Si s states dominate there. The second part (from −6 to −1 eV) represents the bonding Mn d and Si p states with the main peak at −2.1 eV. Finally, the third part (from −1 eV to the Fermi level) is mostly characterized by the nonbonding Mn d states with the narrow peak at −0.3 eV. The shape of the total DOS and features in the projected DOS of Mn_4Si_7 are very close to those of semiconducting $ReSi_{1.75}$.[21]

TABLE II. The principle-axis components of the effective-mass tensor for holes (in the Γ point) and electrons (in the Z point) in units of the free-electron mass (m_0). Because of the tetragonal symmetry, the m_{xx} and m_{yy} components are identical.

Holes		Electrons	
m_{xx}	m_{zz}	m_{xx}	m_{zz}
1.64	5.72	8.17	3.40

We have also evaluated the effective mass tensor for electrons and holes for Mn_4Si_7 at the band extrema along the main crystallographic axes. The masses of the electrons were calculated at the conduction band minimum in the Z point, while the masses of holes at the valence band maximum in the center of the Brillouin zone (the Γ point). The components of the carrier effective mass tensor are represented in Table II. One can observe strong anisotropy both for masses of electrons and holes along different axes. Large values of some components of the effective mass tensor, namely, m_{xx} (m_{zz}) for holes, (electrons) are caused by small dispersion of the bands along the corresponding directions [Fig. 3(a)]. The theoretical values obtained are smaller than the experimentally observed ones (hole effective masses were estimated in Ref. 11 as $m_{xx}=11m_0$ and $m_{zz}=15m_0$; average hole effective mass of $12m_0$ was found in Ref. 9). This discrepancy can be explained by the fact that the estimates were based on the experimental transport data performed for the imperfect crystals or polycrystalline samples also assuming the reduced gap of 0.40 eV due to the presence of defects. Nevertheless, we have also obtained that the hole effective mass along the c direction is considerably larger than the one in the perpendicular direction.

The hole mobility of the nondegenerate semiconducting phase (Mn_4Si_7) of HMS was also estimated. If one assumes the contributions of different scattering mechanisms to be independent, the total mobility according to the Mathiessens approximation is

$$\mu^{-1} = \sum_i \mu_i^{-1},$$

where i stands for different scattering mechanisms under consideration. In our case, we have accounted for the following scattering mechanisms:

$$\mu^{-1} = \mu_{AC}^{-1} + \mu_{NPO}^{-1} + \mu_{PO}^{-1} + \mu_{IM}^{-1} + \mu_0^{-1},$$

where μ_{AC}, μ_{NPO}, μ_{PO}, μ_{IM}, and μ_0 are the carrier mobilities due to scattering by acoustic lattice mode, nonpolar and po-

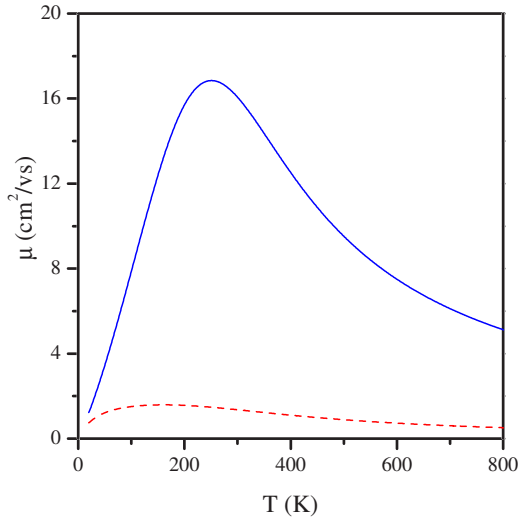

FIG. 6. (Color online) Mobility μ versus temperature T for Mn_4Si_7. The solid line demonstrates the hole mobility for perfect crystals, the dashed one, the mobility of the defected material. We used the following set of parameters in the calculations: the material density to be 5.186 g/cm^{-3}, the mean longitudinal sound velocity, the constant defined by components of the deformational potential tensor and the Debye temperature estimated to be 8.2×10^5 cm/s, 10 eV, and 600 K, respectively, the high frequency and static dielectric constants obtained from our results to be 5 and 30, respectively, and the ionized impurity concentration to be 3×10^{19} cm^{-3}.

lar optical modes, and charged and neutral impurities, respectively. The details of the calculations for each separate mechanism can be found elsewhere.[25] The models used in the present work were successfully applied to various semiconducting silicides showing good correlation with available experimental data.[26–30] The calculated mobility of holes with the averaged effective mass value ($2.49m_0$) for the reasonable set of parameters is shown in Fig. 6. At low temperature range, the scattering by charge impurities mainly defines the mobility rise behavior. However, the behavior can differ from the $\sim T^{3/2}$ one due to the increasing role of the other mechanisms with temperature. On the other hand, at high temperature range, the scattering by phonons is dominant. It is worthwhile to note that the presence of the high defect concentration (neutral impurities) can rather smooth this behavior over the whole temperature range considered. Our theoretical estimates indicate that the difference in the hole mobility for rather perfect crystals with a low value of neutral impurities (10^{18} cm^{-3}, the solid line) as compared to the one with the high defect concentration (10^{20} cm^{-3}, the dashed line) can be significant (reaching an order of magnitude). Accounting for the high value of the neutral impurity concentration allows one to generally reproduce the experimental data for HMS.[8–11] Thus, we suppose that the experimentally observed large effective mass values as well as small carrier mobilities may be caused by the possible structural defects in HMS in addition to the strong degeneracy.[8] To clarify the point, the data of precise measurements on perfect crystals are needed.

By means of the FLAPW method, dependences of the imaginary (ε_2) and real (ε_1) parts of the dielectric function on the photon energy are calculated and are shown in Fig. 7. It is clearly seen that the optical functions display some anisotropy effects. In fact, in the case of the imaginary part of the dielectric function (Fig. 7, left panel), the magnitude of the main peak at about 1.5 eV is sizably larger for the **E**$\|$**zz** light polarization than the one for the **E**$\|$**xx** light polarization. In addition, the **E**$\|$**zz** curve has a shoulder at 2.5 eV, which is not present in the **E**$\|$**xx** curve. At the range of 4–6 eV, both curves possess the second maximum at 5 eV displaying almost the same magnitude. We believe that the dipole matrix elements are responsible for such a difference in the magnitude of the main peak of ε_2 at 1.5 eV. We have checked the dipole matrix elements of transitions of about 1.5 eV across the gap and found out that they mostly had larger values for the **E**$\|$**zz** light polarization with respect to the **E**$\|$**xx** one. Another issue worthwhile to discuss is the very small values of the dipole matrix elements of the first direct transitions in the Γ and Z points [Fig. 3(a)]. It is clearly seen that the rapid start of the ε_2 curves is at 0.91 eV (compare to the first direct transitions of 0.77–0.79 eV) indicating that such a rapid increase is due to higher lying transitions with appreciable oscillator strength and the joint density of the interband states. The reason why the first direct transitions display small values of the dipole matrix elements can be the Mn d states dominating across the gap (see the projected DOS in Fig. 5), which is typical of transition metal silicides.[22,31–33] In the case of the real part of the dielectric function (Fig. 7, right panel), similar anisotropy ef-

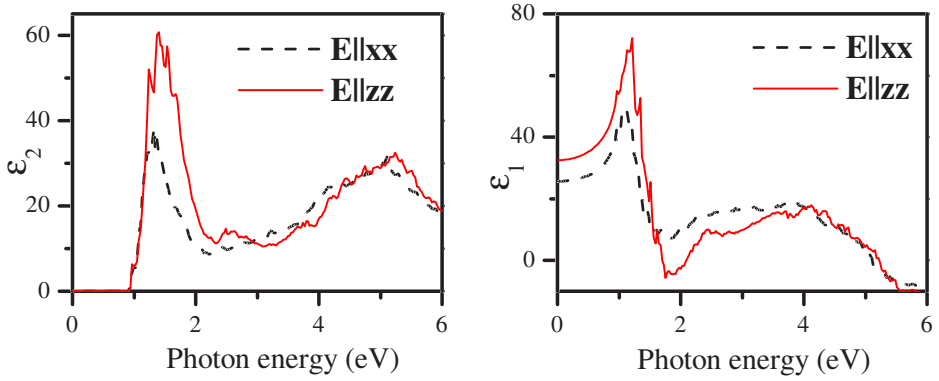

FIG. 7. (Color online) The imaginary (ε_2) and real (ε_1) parts of the dielectric function of Mn_4Si_7 versus photon energy for different light polarizations.

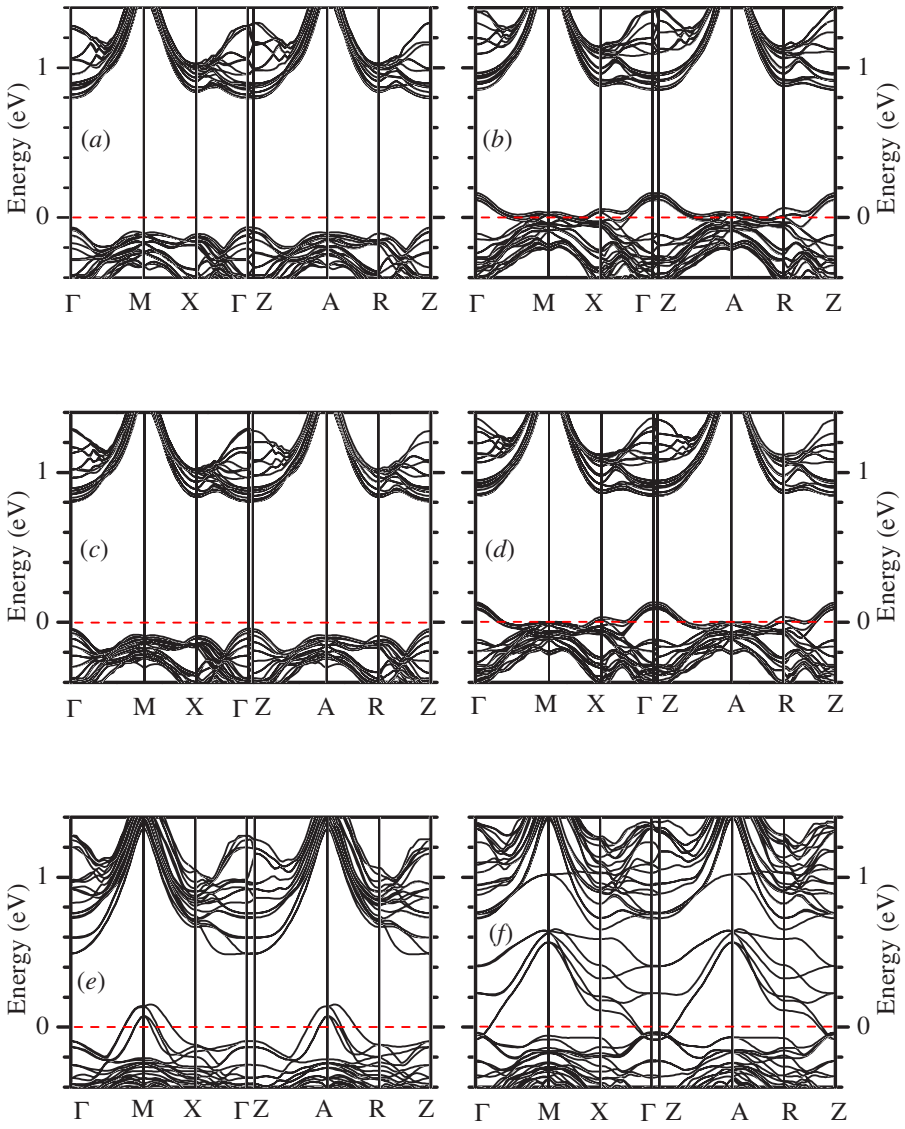

FIG. 8. (Color online) The spin-dependent band structures of [(a) and (b)] $Mn_{11}Si_{19}$, [(c) and (d)] $Mn_{15}Si_{26}$, and [(e) and (f)] Mn_4Si_7 with stacking fault. The left and right panels correspond to the majority-spin and minority-spin cases, respectively. Zero at the energy scale indicates the Fermi energy.

fects for different light polarizations can be easily spotted. We also notice that the static dielectric constant $\varepsilon_1(0)$ is about 26 and 33 for the $\mathbf{E}\|\mathbf{xx}$ and $\mathbf{E}\|\mathbf{zz}$ light polarizations, respectively. In our calculations of the dielectric function, we did not take into account a real electron-hole excitation which is known to provide a better description of optical properties.[34] However, in the case of β-$FeSi_2$, we have already shown that our method has calculated ε_2 and ε_1 in perfect agreement with experimental data.[32] The latter issue was attributed to the dielectric screening. For HMS, we also expect the screening effects to attenuate the electron-hole interaction. In fact, comparison with ellipsometry results for HMS (see Fig. 2 of Ref. 15) indicates that we reproduce very well the shape and features in the ε_2 and ε_1 dependences on photon energy.

In the cases of $Mn_{11}Si_{19}$, $Mn_{15}Si_{26}$, and $Mn_{27}Si_{47}$, the metal-like behavior of ε_2 and ε_1 at low photon energies is expected and, actually, observed[13] because of the free carrier absorption due to the partly occupied valence band [Figs. 3(b)–3(d)]. However, at higher photon energies, these phases should display the shape of the dielectric function close to that of Mn_4Si_7. The latter statement can be easily understood by taking into consideration the following facts. All HMSs are characterized by similar dispersion of the bands close to the gap. Moreover, the excluded contributions from transitions across the gap involving the unoccupied part of the valence band are not significant because this unoccupied part is small and the Mn *d* states prevail in the energy range near the gap that, in turn, would provide very low oscillator strength of such transitions. Therefore, the Mn_4Si_7 phase can be considered as a model phase to describe optical properties of HMS.

D. Spin-polarized calculations of higher manganese silicides

We have performed spin-polarized calculations of Mn_4Si_7, $Mn_{11}Si_{19}$, and $Mn_{15}Si_{26}$ by means of the USPP method. The

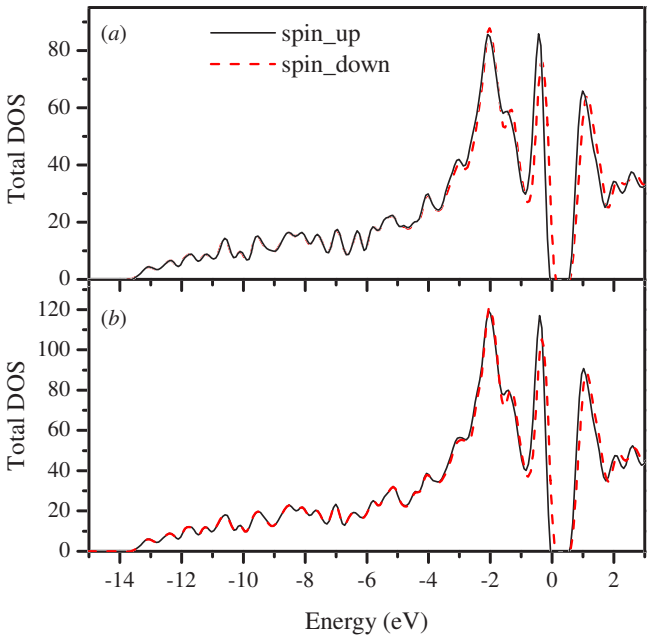

FIG. 9. (Color online) The spin-dependent total DOS (states/eV/cell) of (a) $Mn_{11}Si_{19}$ and (b) $Mn_{15}Si_{26}$. Zero at the energy scale corresponds to the Fermi energy.

Mn_4Si_7 phase does not show any magnetic moment, while the $Mn_{11}Si_{19}$ and $Mn_{15}Si_{26}$ phases display very small ones which have turned out to be $0.10\mu_B$/Mn and $0.08\mu_B$/Mn, respectively. The total energy difference between the nonmagnetic and ferromagnetic states in the case of $Mn_{11}Si_{19}$ and $Mn_{15}Si_{26}$ is found to be marginal and quite comparable with the accuracy of the method. The latter fact makes it difficult to unambiguously identify the ground state. The spin-dependent band structures of $Mn_{11}Si_{19}$ and $Mn_{15}Si_{26}$ are shown in Fig. 8. It is clearly seen that both phases for the majority-spin and minority-spin bands have the energy gap. However, the majority-spin band is semiconducting (0.06 and 0.04 eV separate the Fermi level and the top of the valence band for $Mn_{11}Si_{19}$ and $Mn_{15}Si_{26}$, respectively) and the minority-spin band is metallic (the Fermi level intersects bands 0.17 and 0.14 eV below the top of the valence band for $Mn_{11}Si_{19}$ and $Mn_{15}Si_{26}$, respectively). In general, dispersion of the bands close to the gap for spin-polarized [Figs. 8(a)–8(d)] and non-spin-polarized [Figs. 3(a)–3(d)] cases is similar, except for the cases with semiconducting nature [Figs. 8(a)–8(c)] where the valence band maxima at the Γ and Z points are not so pronounced and shifted down in energy. All spin-dependent bands with the metallic character [Figs. 8(b)–8(d)] display the direct energy gap of 0.70 eV in the Γ and Z points, and the bands with the semiconducting behavior [Figs. 8(a)–8(c)] possess the direct band gap of 0.85 eV in the Γ and Z points. In Fig. 9, we report the spin-polarized total DOSs of $Mn_{11}Si_{19}$ and $Mn_{15}Si_{26}$ which shape is almost identical to the one of the nonmagnetic Mn_4Si_7 phase (Fig. 5). A relatively small exchange splitting can only be observed near the Fermi level between the majority-spin and minority-spin bands mainly composed of the Mn d states (Fig. 5). To this end, we believe that the $Mn_{27}Si_{47}$ phase would also display a weak ferromagnetism like the $Mn_{11}Si_{19}$ and $Mn_{15}Si_{26}$ phases.

As we have mentioned above, for $Mn_{11}Si_{19}$ and $Mn_{15}Si_{26}$, the spin-dependent bands display both metallic and semiconducting characters that are typical of half-metals. The latter ones (Heusler alloys,[35] some oxides,[36] transition metal chalcogenides[37]) are promising for spintronic applications[38] because they provide only one electronic spin character at the Fermi energy with the 100% spin polarization. The origin of the gap was shown to stem from the strong hybridization between the d states of transition metal atoms leading to the large exchange splitting. However, in our case of HMS, the gap was originally present with the Fermi energy just below the top of the valence band [Figs. 3(b)–3(d)] and a rather small exchange splitting was enough to display the half-metallic character [Figs. 8(a)–8(d)]. Thus, the energy gaps for spin excitation of holes are 0.06 and 0.04 eV in the case of the $Mn_{11}Si_{19}$ and $Mn_{15}Si_{26}$ phases, respectively. Even though the high quality thin films of HMS can be grown on silicon substrate,[39,40] the low Curie temperature (40 K)[2] and the existence of several phases of HMS with half-metal and semiconducting properties would probably limit applications of these silicides for spintronics.

Gottlieb *et al.*[2] reported the Mn_4Si_7 phase to be a weak itinerant magnetic system. However, our calculations have shown that this phase has zero magnetic moment and the nonmagnetic ground state. One possible explanation to this discrepancy can be the presence of several phases of HMS[7,8] which may eventually provide nonzero magnetic moment. Another possibility worthwhile to consider is a stacking fault in the crystal structure of Mn_4Si_7. We have performed the spin-polarized calculation of the Mn_4Si_7 phase with stacking faults and have revealed that the ferromagnetic state was the ground state of this phase displaying the magnetic moment of $0.24\mu_B$/Mn. The corresponding band diagrams are shown in Figs. 8(e) and 8(f). Our calculations of the Mn_4Si_7 phase with stacking faults are based on an ideal structural model, however, we would like to point out that stacking faults can affect magnetic properties of HMS.

IV. CONCLUSIONS

Our study has shown the degenerate semiconducting nature of $Mn_{11}Si_{19}$, $Mn_{15}Si_{26}$, and $Mn_{27}Si_{47}$, which is found to be an intrinsic feature of their band structures. This fact clarifies very well the measured resistivity variation with temperature[9–11] typical of degenerate semiconductors. These phases also possess similar band dispersion near the energy gap, which makes it difficult to distinguish between them by means of resistivity and optical measurements. In addition, the spin-polarized calculations of $Mn_{11}Si_{19}$ and $Mn_{15}Si_{26}$ have revealed half-metallic properties with the possibility to provide 100% spin polarization of holes at the Fermi energy. Mn_4Si_7 shows the semiconducting character displaying the indirect and the direct band gaps of 0.77 and 0.79 eV, respectively, and sizable anisotropy in the dielectric function. We have also found stoichiometry of HMS to define their

degeneracy: only HMSs with the $MnSi_{1.75}$ stoichiometry are not degenerate semiconductors. We have suggested that stacking faults can be a possible cause of a decrease of the band gap to 0.40 eV observed in optical[8,15] and transport[9–11] experiments.

ACKNOWLEDGMENTS

We thank A. L. Danilyuk, N. A. Poklonski, and M. G. Lukashevich for the fruitful discussion and useful suggestions on the results of the paper.

*migas@mater.unimib.it

[1] *Semiconducting Silicides*, edited by V. E. Borisenko (Springer, Berlin, 2000).
[2] U. Gottlieb, A. Sulpice, B. Lambert-Andron, and O. Laborde, J. Alloys Compd. **361**, 13 (2003).
[3] O. Schwomma, H. Nowotny, and A. Wittman, Monatsch. Chem. **94**, 681 (1963).
[4] O. Schwomma, A. Preisinger, H. Nowotny, and A. Wittman, Monatsch. Chem. **95**, 1527 (1964).
[5] H. W. Knott, M. H. Mueller, and L. Heaton, Acta Crystallogr. **23**, 549 (1967).
[6] G. Zwilling and H. Nowotny, Monatsch. Chem. **104**, 668 (1973).
[7] H. Q. Ye and S. Amelincks, J. Solid State Chem. **61**, 8 (1986).
[8] S. Teichert, R. Kilper, J. Erben, D. Franke, B. Gebhard, T. Franke, P. Haussler, W. Henrion, and H. Lange, Appl. Surf. Sci. **104-105**, 679 (1996).
[9] I. Nishida, J. Mater. Sci. **7**, 435 (1972).
[10] C. Krontiras, K. Pomoni, and M. Roilos, J. Phys. D **21**, 509 (1988).
[11] I. Kawasumi, M. Sakata, I. Nishida, and K. Masumoto, J. Mater. Sci. **16**, 355 (1981).
[12] G. V. Samsonov, *Plenum Press Handbooks of High-Temperature Materials, No. 2: Properties Index* (Plenum, New York, 1964), p. 161.
[13] M. C. Bost and J. E. Mahan, J. Electron. Mater. **16**, 389 (1987).
[14] L. Zhang and D. G. Ivey, J. Mater. Sci.: Mater. Electron. **2**, 116 (1991).
[15] M. Rebien, W. Henrion, H. Angermann, and S. Teichert, Appl. Phys. Lett. **81**, 649 (2002).
[16] G. Kresse and J. Hafner, Phys. Rev. B **49**, 14251 (1994).
[17] G. Kresse and J. Furthmüller, Comput. Mater. Sci. **6**, 15 (1996).
[18] G. Kresse and J. Furthmüller, Phys. Rev. B **54**, 11169 (1996).
[19] J. P. Perdew and Y. Wang, Phys. Rev. B **45**, 13244 (1992).
[20] P. Blaha, K. Schwarz, G. K. H. Madsen, D. Kvasnicka, and J. Luitz, *WIEN2k, An Augmented Plane* Wave+Local *Orbitals Program for Calculating Crystal Properties* (Karlheinz Schwarz, Technische UniversitatWien, Austria, 2001).
[21] A. B. Filonov, D. B. Migas, V. L. Shaposhnikov, N. N. Dorozhkin, V. E. Borisenko, H. Lange, and A. Heinrich, Europhys. Lett. **46**, 376 (1999).
[22] V. L. Shaposhnikov, A. V. Krivosheeva, L. I. Ivanenko, A. B. Filonov, V. E. Borisenko, M. Rebien, W. Henrion, D. B. Migas, L. Miglio, G. Behr *et al.*, J. Phys.: Condens. Matter **16**, 303 (2004).
[23] E. G. Moroni, W. Wolf, J. Hafner, and R. Podloucky, Phys. Rev. B **59**, 12860 (1999).
[24] F. L. Via, M. G. Grimaldi, D. B. Migas, and L. Miglio, Appl. Phys. Lett. **78**, 739 (2001).
[25] B. K. Ridley, *Quantum Processes in Semiconductors* (Clarendon, Oxford, 1982).
[26] A. B. Filonov, I. E. Tralle, D. B. Migas, V. L. Shaposhnikov, and V. E. Borisenko, Phys. Status Solidi B **203**, 183 (1997).
[27] L. Ivanenko, V. L. Shaposhnikov, A. B. Filonov, D. B. Migas, G. Behr, J. Werner, J. Schumann, H. Vinzelberg, and V. Borisenko, Microelectron. Eng. **64**, 225 (2002).
[28] L. Ivanenko, A. Filonov, V. Shaposhnikov, G. Behr, D. Souptel, J. Schumann, H. Vinzelberg, A. Plotnikov, and V. Borisenko, Microelectron. Eng. **70**, 209 (2003).
[29] L. I. Ivanenko, V. L. Shaposhnikov, A. V. Krivosheeva, A. B. Filonov, V. E. Borisenko, D. B. Migas, L. Miglio, G. Behr, and J. Schumann, Thin Solid Films **461**, 141 (2004).
[30] D. B. Migas, V. L. Shaposhnikov, A. B. Filonov, N. N. Dorozhkin, and V. E. Borisenko, J. Phys.: Condens. Matter **19**, 346207 (2007).
[31] D. B. Migas, L. Miglio, V. L. Shaposhnikov, and V. E. Borisenko, Phys. Status Solidi B **231**, 171 (2002).
[32] D. B. Migas, L. Miglio, W. Henrion, M. Rebien, F. Marabelli, B. A. Cook, V. L. Shaposhnikov, and V. E. Borisenko, Phys. Rev. B **64**, 075208 (2001).
[33] D. B. Migas, V. L. Shaposhnikov, V. N. Rodin, N. N. Dorozhkin, and V. E. Borisenko, Phys. Status Solidi B **244**, 3178 (2007).
[34] M. Rohlfing and S. G. Louie, Phys. Rev. B **62**, 4927 (2000).
[35] I. Galanakis, P. Mavropoulos, and P. H. Dederichs, J. Phys. D **39**, 765 (2006).
[36] J. R. J. Soulen, J. M. Byers, M. S. Osofsky, B. N. B. T. Ambrose, S. F. Cheng, P. R. Broussard, C. T. Tanaka, J. Nowak, J. S. Moodera *et al.*, Science **282**, 85 (1998).
[37] W. H. Xie, Y. Q. Xu, B. G. Liu, and D. G. Pettifor, Phys. Rev. Lett. **91**, 037204 (2003).
[38] I. S. Osborne, Science **294**, 1483 (2001).
[39] H. Tatsuoka, T. Koga, K. Matsuda, Y. Nose, Y. Souno, H. Kuwabara, P. D. Brown, and C. J. Humphreys, Thin Solid Films **381**, 231 (2001).
[40] S. Teichert, H. Hortenbach, and H. J. Hinneberg, Appl. Phys. Lett. **78**, 1988 (2001).